



Fiber optic probe with functional polymer composites for hyperthermia

ALEXA HERNÁNDEZ-ARENAS,¹ REINHER PIMENTEL-DOMÍNGUEZ,¹ J. RODRIGO VÉLEZ-CORDERO,² AND JUAN HERNÁNDEZ-CORDERO^{1,*} 

¹*Instituto de Investigaciones en Materiales, Universidad Nacional Autónoma de México, Ciudad Universitaria, Mexico City 04510, Mexico*

²*Instituto de Física-Cátedras CONACyT, Universidad Autónoma de San Luis Potosí, San Luis Potosí 78290, San Luis Potosí, Mexico*

*jhcordero@iim.unam.mx

Abstract: We demonstrate a fiber optic probe incorporating functional polymer composites for controlled generation of photothermal effects. The probe combines carbon-based and rare-earth composites on the tip of standard multimode fibers, thus yielding a compact fiber optic photothermal probe (FOPP) whose temperature can be measured simultaneously through fluorescent thermometry. We evaluate the thermal features of the probe through experiments and numerical calculations showing that large thermal gradients are obtained within the vicinity of the heating zone. The temperatures achieved with the FOPP are within the ranges of interest for hyperthermia and can be attained using low optical powers (< 280 mW).

© 2021 Optical Society of America under the terms of the [OSA Open Access Publishing Agreement](#)

1. Introduction

Several types of cancer therapies have emerged in the medical field, being radiotherapy, chemotherapy and surgery the most used treatments against this disease. Yet, in the incessant struggle to improve the quality of life of cancer patients, new treatment alternatives have emerged aiming at reducing secondary effects while improving the effectiveness of tumor elimination. Particularly, treatments based on heat generation can induce different physiological effects leading to size reduction of tumoral tissue, as well as death or even annihilation of cancerous cells [1–6]. Target specificity or spatial selectivity of these types of treatments can vary from low to high, depending on the device used to generate heat. Typically, devices for thermal therapy are based on radiofrequency electrodes, microwave antennas or ultrasound transducers, providing different methods with different degrees of invasiveness for therapeutic heat delivery [1,7].

Optical radiation is a highly attractive option for rapidly heating small spatial regions. Lasers in particular allow for heating tissue with high spatial and temporal resolution thus offering a means to perform light-driven thermal therapy. This type of anti-cancer treatment is known as photothermal therapy or PTT (also called laser thermotherapy), and can produce an adequate increase in temperature to cause irreversible damage to tumoral cells [5,8]. Most of the current PTT procedures rely on optical absorption by the target tissue and the laser wavelength must therefore overlap with the absorption bands of the endogenous chromophores (e.g., water, blood or melanin). A limitation of this approach is that the photothermal efficiency (i.e., optical power to heat conversion) depends completely on the optical absorption features of the tissue. Hence, PTT for low absorption tissues requires high-power lasers (typically >1 W output power) and extended exposure times (normally several minutes) to achieve the desired thermal effect [9]. An alternative to absorption by endogenous chromophores is the use of exogenous chromophores with high optical absorption that must be delivered to the target tissue. Nanomaterials such as metallic or carbon nanoparticles have been effectively used as light-activated “nano-heaters” owing to their enhanced optical absorption [10–14]. These engineered nanoparticles require lower

optical powers and short irradiation times (seconds) to trigger cell death and their effectiveness to combat various types of cancer, in both *in vitro* and *in vivo* studies, has been reported previously [15–18]. Thus, the use of nanomaterials with photothermal features has opened new possibilities for PTT.

Light delivery for PTT is typically done with optical fibers, particularly for tumors allocated in intricate regions of the body. This is the so-called interstitial thermotherapy, in which the fibers are guided by needles or catheters, and has been proven useful for treating inoperable or deep-seated brain tumors [6,19–21]. In addition to light delivery, temperature monitoring and precise control of the generated heat are other important aspects that need to be considered in an efficient PTT procedure [2–5,8,22]. Although several techniques for temperature monitoring during PTT are available [23,24], thermocouples, thermistors and fiber optic sensors (FOTS) are the preferred choice for interstitial procedures [9,25–28]. In general, these devices show adequate features (i.e., compact size and sensitivity) for interstitial PTT, but care should be taken with the location of the sensor with respect to the photothermal element as strong temperature gradients are typically observed in PTT procedures [29,30]. This is important because the temperature registered by the sensor will not necessarily correspond to the actual temperature reached by the photoactive element and will not coincide with the temperature reached at the target point either. In contrast to commercial probes incorporating thermistors for temperature measurements [31,32], recent developments of PTT probes incorporate fiber optic sensors aiming at minimizing errors in temperature measurements. For instance, fiber Bragg gratings as well as Fabry-Pérot devices have been successfully incorporated as sensors in fiber optic-based PTT probes [25–28,33–38], thus providing a means to integrate light delivery capabilities and temperature measurements within a single device. Furthermore, their reduced size and performance address key aspects in the design of photothermal probes such as spatial selectivity, on-target heat generation and on-target temperature monitoring.

In this paper we introduce a novel photothermal probe based on optical fibers and polymer composites. Instead of relying on light delivery and absorption of the target tissue for heating, the proposed fiber-optic photothermal probe (FOPP) allows for delivering heat directly on the target zone. The probe uses a silica multimode optical fiber tip incorporating two photoactive polymer composites placed in series: one based on carbon nanopowder (CNP) for heat generation and one with rare-earth powders for fluorescence temperature measurements. While the latter has been demonstrated as a suitable material for fiber optic temperature sensors [39], the polymer composite incorporating CNPs has shown to be useful for developing photothermal membranes and coatings [40]. The configuration of the probe allows for pumping both composites with a single laser diode, effectively increasing the temperature of the probe at adequate levels for hyperthermia with optical powers in the milliwatts range. We present a numerical and experimental characterization of the FOPP showing the highly localized thermal effect generated with the device. The thermal gradients in the vicinity, which are relevant for hyperthermia, are also analyzed considering the thermal properties of the surrounding medium. Our results show that the FOPP offers excellent features for hyperthermia applications, including spatial selectivity and the possibility to set the temperature to a fixed value through the optical power of the laser diode.

2. Probe design and fabrication

2.1. Materials

The proposed fiber-optic photothermal probe (FOPP) incorporates the polymer composites and a dual-fiber tip allocated in a glass capillary, as shown in Fig. 1. Two standard multimode optical fibers (62.5 μm core diameter) are used for the dual-fiber tip, obtained upon fusing the two fiber claddings with a coupler manufacturing station (Dowson Corp., model OC2010). The tip is then inserted and glued in a standard 21G needle to provide mechanical strength to the fibers. This reinforced fiber tip is then inserted into a glass capillary (O.D. 1.6mm, I.D. 1.0mm) for allocating

the polymer composites as described below. Since the cores of the fibers are not fused, one of them serves for pumping the composites and the other for collecting the fluorescence from the temperature sensitive polymer.

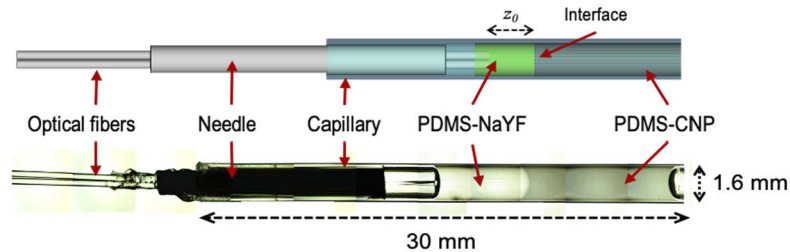


Fig. 1. Configuration of the polymeric photothermal probe: schematic representation (top), and image of the actual device showing its characteristic dimensions (bottom). The probe is composed of a temperature sensitive composite (PDMS-NaYF) and a photothermal composite (PDMS-CNP) enclosed in a glass capillary.

Heating of the probe is achieved by means of the photothermal composite, fabricated following a similar procedure to that reported previously [40]. Briefly, carbon nanopowder (Sigma Aldrich, 633100) was incorporated in pristine PDMS (Dow Corning, Sylgard 184) with a concentration of 0.05% in weight, adding chloroform to reduce cluster formation. This blend was mixed with a magnetic stirrer while heating at 70 °C until the chloroform was evaporated. Next, the curing agent for the PDMS was incorporated in a 1:10 ratio and mixed by hand for 5 minutes. Incorporation of the CNP in PDMS following this process provides a simple means to obtain a polymer composite with photothermal effects, arising from the optical absorption by the carbon nanoparticles. Heat is generated within the composite in a highly efficient manner, allowing for using a laser diode as a pump source to obtain a temperature increase of up to a few hundred degrees (°C) with optical powers in the milliwatts range [40]. Furthermore, since the temperature increases linearly with the optical power, the temperature in the composite can be adjusted upon controlling the laser power.

A similar mixing procedure was followed to obtain the temperature sensitive polymer composite. As described in a previous report [39], sodium yttrium fluoride powder doped with Er^{+3} and Yb^{+3} ($\text{NaY}_{0.77}\text{Yb}_{0.20}\text{Er}_{0.03}\text{F}_4$, Sigma Aldrich 756555) was incorporated into PDMS in a 1% per weight concentration. The curing agent for the PDMS was then added to the mixture and mixed by hand for 3 min. The rare earth-doped sodium powder absorbs in the wavelength range of 940–980 nm and provides high up-conversion (UC) luminescence efficiencies in the green portion of the visible spectrum [39]. Upon mixing it with the PDMS, the resulting fluorescent composite generates green UC emission whose spectral features are temperature dependent. Spectral analysis can thus be used for monitoring temperature changes in the composite; in particular, we used the fluorescence intensity ratio (FIR) technique, based on obtaining the temperature changes through the ratio of the emission bands of two thermally coupled energy levels. The PDMS-NaYF composite has shown an excellent performance as sensing material for fiber optic sensors and can be suitably pumped with a laser diode [39].

2.2. Methods

As shown in Fig. 1, both polymer composites are allocated in series inside the glass capillary. The photothermal composite (PDMS-CNP) was poured first into the capillary and then cured at 90 °C for 2 hours. Subsequently, the fluorescent polymer composite (labelled as PDMS-NaYF) was poured into the same glass capillary over the already cured PDMS-CNP photothermal composite. The metallic needle containing the dual-fiber tip was then inserted into the glass

capillary verifying that the fibers were immersed in the PDMS-NaYF composite. After proper alignment of the fiber tip, the assembled probe was finally heated at 90 °C for 2 hours to cure the PDMS-NaYF section. As shown in Fig. 1, the final FOPP has approximately 30 mm in length and a diameter of 1.6 mm, corresponding to the outer diameter of the glass capillary basket. This relatively small sized probe can be inserted inside a 13G needle, for example, and therefore contribute to the overall goal of having a minimally invasive device for therapeutic procedures.

2.3. Setup for probe pumping and fluorescence temperature measurements

The setup used with the FOPP for heating and temperature monitoring includes an infrared diode laser (975 nm, 330 mW, Thorlabs) and a solid-state spectrometer (Ocean Optics, USB4000). As shown in Fig. 2, one of the fibers of the dual tip is used for pumping the FOPP while the remaining fiber is used to collect the fluorescence of the temperature sensitive composite. When the laser diode (LD) is turned on, the pump radiation is first absorbed by the fluorescent PDMS-NaYF composite and the generated green UC signal is analyzed by means of the spectrometer. The residual pump radiation then reaches the PDMS-CNP composite increasing the temperature of the probe through the photothermal effect. A virtual instrument programmed in *LabView* was used to acquire and analyze the spectra from the fluorescent composite yielding a temperature readout from the FOPP. The temperature calibration for the fluorescent signal from the PDMS-NaYF composite was carried out as described in [39]. Since the FIR technique relies on the ratio of two fluorescence bands, the resulting temperature readings are insensitive to variations of the pump signal. Thus, the laser diode power can be increased to raise the temperature of the photothermal composite and the temperature reading will track the temperature of the probe accordingly. With this serial arrangement of both polymer composites, we therefore expect to obtain FIR-based temperature measurements very close to the maximum temperature generated by the photothermal polymer. Since most of the residual pump is absorbed in a very short length of the PDMS-CNP composite, we expect to achieve the maximum temperatures within the vicinity of the interface between both polymer composites (see Fig. 1).

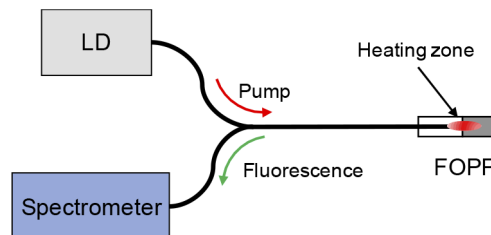


Fig. 2. Setup for the heating and temperature monitoring with the fiber optic photothermal probe (FOPP). A laser diode (LD) is used for pumping both, the fluorescent (PDMS-NaYF) and the photothermal (PDMS-CNP) polymer composites. The fluorescence signal is used for temperature measurements through spectral analysis (see text for details).

3. Heat generation simulations

As a first step, the thermal features of the FOPP were assessed by means of computer simulations. We were interested particularly in evaluating the temperature gradients in the vicinity of the photothermal composite. This is relevant as it provides an estimate of the correspondence between the temperature reading obtained with the probe and the actual temperature at the target point. The latter, in addition, is influenced by the thermal properties of the target tissue itself (surrounding media). Thus, the numerical simulations seek to provide an estimation of the thermal properties of the probe and hence predict its performance when located within any heat

dissipative media. The simulations were further used to explore the feasibility to obtain the temperature at any point around the probe using as reference the temperature reported by the sensor, i.e., the PDMS-NaYF composite. The geometrical model used in these simulations is shown in the schematic of Fig. 1, describing the main components of the FOPP together with their relevant dimensions: the section containing the fluorescent composite (PDMS-NaYF), the portion of the probe containing the photothermal composite (PDMS-CNP), a capillary glass tube and a stainless-steel needle used to guide and support the optical fibers. The thermal transport properties of these materials were all included in the simulations, with the exception of those corresponding to the dual optical fiber tip, which were not considered because its thickness (150 μm) is much smaller than any other length scale considered in the model.

The heat transfer equation was solved in this geometrical model using axisymmetric cylindrical coordinates with the origin located at the tip of the dual optical fibers. We used a ray optics-like representation in order to compute the heat generated by the PDMS-CNP composite due to absorption of the near-infrared laser diode radiation. Refractive effects within the probe were considered using Snell's law at the boundaries between media with different refractive indices (n_i). We further considered that the intensity of the beam coming out from the optical fiber core has a divergent Gaussian distribution. Under these conditions, the overall problem then reduces to solving the steady-state energy equation (transient when indicated):

$$\nabla \cdot (-k \nabla T) = Q_{gen} \quad (1)$$

having a heat generation term of the form

$$Q_{gen} = \eta_{eff} \kappa_2 I_0 e^{[-\kappa_2(Z-Z_0) - r^2/A]} \quad (2)$$

where

$$A = w^2/2, \quad I_0 = P_0 e^{-\kappa_1 z_0} / (A\pi) \quad (3)$$

The beam radius $w=w(z)$ can be included in the model using piecewise functions in order to consider refraction of the light path. Specifically, when light comes out from the optical fiber, w can be computed as:

$$w = w_0 + z \tan(\theta) \quad (4)$$

where the angle θ is related to the numerical aperture of the fiber. In the above equations $T(r, z)$ is the temperature, κ_i is the extinction coefficient of the PDMS-NaYF ($i = 1$) and the PDMS-CNP ($i = 2$) sections, k is the thermal conductivity, P_0 is the optical power and $w_0 \sim 18.75 \mu\text{m}$ is the core radius of the optical fiber. The term Q_{gen} is applied only inside the region comprised by the PDMS-CNP composite, i.e., we neglected any other absorption mechanism linked to the generation of heat. Additionally, the pump intensity arriving at the photothermal composite is represented by I_0 in eq.3; notice that this already accounts for the absorption by the PDMS-NaYF fluorescent composite (i.e., the sensing region) whose length from the fiber's tip to the composites interface is denoted as z_0 (see Fig. 1).

The term η_{eff} in eq.2 is the photothermal conversion efficiency and includes all the processes that may reduce the optical intensity aside from absorption (e.g., scattering or reflection) and are not involved in the increase in temperature. η_{eff} is in fact the only unknown parameter in all equations, as the extinction coefficients $\kappa_1 = 0.178 \text{ mm}^{-1}$ and $\kappa_2 = 0.488 \text{ mm}^{-1}$ were measured experimentally from the composites. We thus calibrated the values of η_{eff} upon comparing the numerical values of the temperatures with those obtained experimentally for a given optical power (P_0). This was done with a set of temperature points measured experimentally in air and water as described below. The values for the thermal conductivities used for the different materials depicted in Fig. 1 are listed in Table 1. Notice that the thermal conductivities vary with temperature (as denoted by the "(T)" notation in the table), and hence only typical values for k

Table 1. Parameters used for the numerical model

Material	Thermal conductivity [W/m K]	Refractive index
Air (T)	0.026	1
Water (T)	0.60	1.3333
Glass	1.40	1.4585
PDMS (with $\text{Er}^{3+}\text{Yb}^{3+}$ or CNP)	0.26	1.4030
Stainless Steel	44.5	—

are included. For our simulations, the thermal conductivities were computed using well-known polynomial state functions, $k = k(T)$.

For the simulations, the computational model of the FOPP, having a total length of ~ 2.8 cm and radius of 0.8 mm, was located inside a box with dimensions of 55×30 mm. This spatial domain enclosed by a box was designated as the dissipative media and essential boundary conditions were applied throughout the whole external surface of this axisymmetric box. Computationally, we used COMSOL Multiphysics 5.0 to solve Eqs. (1) and (2) using the default shape functions (quadratic Legendre polynomials) for $T(r, z)$. The solver also includes a Newton-Raphson step for handling the non-linear terms, such as the dependence of k with the temperature ($k = k(T)$). Closer to the vicinity of the probe, a mesh refinement factor of 20 was used to reduce the size of the triangular elements and improve the accuracy of the results near the heat generation region. Further increase of the numerical box or mesh refinement factor did not changed the results more than 0.5%.

As a final note on the numerical model, notice that one should decide as well on how to compare the experimental values of the temperature obtained by the PDMS-NaYF composite (i.e., the sensor within the probe), with the temperature values obtained with the simulations. An obvious choice is to take the temperature average in the numerical region occupied by this composite. However, as we will show later, a better choice is actually taking the temperature average at the interface (surface area of 0.78 mm^2) between the PDMS-NaYF and the PDMS-CNP computational domains.

4. Probe characterization

Figure 3 shows experimental results of the temperature increase as a function of the optical power obtained when the FOPP was surrounded by air. The temperature was determined through FIR analysis of the PDMS-NaYF fluorescence spectra, and was registered simultaneously with a sharp-point thermocouple (TC, K-type, Omega 5TC-TT-KI) located sideways just outside the probe, touching the glass casket at the composites' interface (see Fig. 1). This configuration allowed for avoiding any potential spurious effects on the temperature readings attributable to light absorption by the TC. The maximum value reached in air as registered by the FOPP was 80°C for a laser diode output power of 250 mW and the rate of temperature increase was $\sim 0.2^\circ\text{C/mW}$, showing that high temperatures can be readily achieved with low optical powers (< 1 W). It is worth noticing that most fiber-based devices relying on optical absorption by the target tissue require optical laser systems with output powers well above 1 W [25,30,36,38]. Figure 3 also shows the increase in temperature as a function of time; after the laser diode is turned on, the temperature increases until reaching a steady value determined by the optical power. Notice that the temperature raises rapidly and within a few seconds it settles at a steady value that can be sustained until the laser is turned off. Remarkably, the temperatures achieved with such low pump powers are within those that have been useful for hyperthermia [5–9]. Perhaps not surprisingly, the temperatures obtained with the probe sensor and the thermocouple do not coincide (see Fig. 3). This is because the PDMS-NaYF composite is closer to the heat generation region.

Notice further that the discrepancies in the temperature readings increase as the temperature increases, as shown in both, the static (a) and transient (b) plots of Fig. 3.

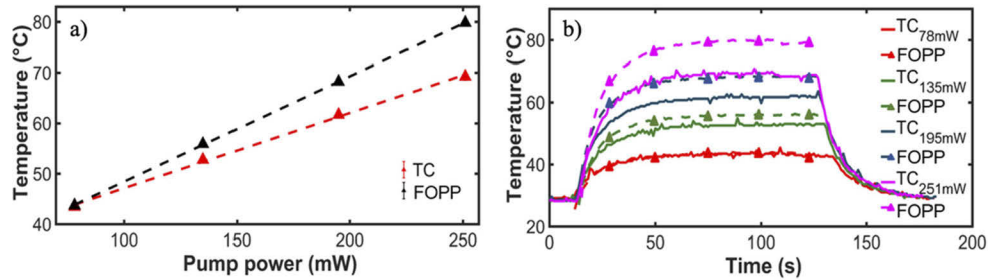


Fig. 3. (a) Temperature of the probe in air as a function of the optical power measured by the fluorescent rare earths-polymer composite (FOPP) and an external thermocouple (TC). (b) Time response of the FOPP compared to the external TC for different optical powers.

In order to obtain a better insight of the temperature distribution in the vicinity of the FOPP, we registered the temperature with the thermocouple (TC) at different locations for a fixed optical power $P_0 \sim 260$ mW. The location of the points at which the temperature was measured is shown in Fig. 4; data for this matrix of points was obtained upon displacing the TC in the radial and axial directions (see Fig. 4) and acquiring the temperature at each point ($T(m, n)$). This was done using air at room temperature (25–27 °C) as the dissipative media, as well as after immersing the probe in water at 36–37 °C. Figure 5 shows the registered temperatures as a function of the radial distance for different axial locations, and Fig. 6 shows the temperatures as a function of the axial distance obtained by displacing the TC along the probe while keeping it in contact with the glass capillary. The radial variation in temperature shows a monotonic decrease as the TC is displaced away from the FOPP (Fig. 5). In contrast, as shown in Fig. 6, the temperature shows a maximum reading near the interface between the two polymer composites (~ 1 mm above the interface on the PDMS-CNP side). As for the effects of the external medium, it is evident from the TC data that the increase in temperature is larger in air compared to water. This is because the thermal conductivity of water is an order of magnitude larger than that of air ($k_{\text{air}} \approx 0.026$ W/m K) thereby hindering heat dissipation effects.

The temperatures registered with the TC were used to calibrate the numerical model and obtain the photothermal conversion efficiency (η_{eff}) of the FOPP. This process involved using temperature data for both dissipative media (i.e., air and water) and obtain the value of η_{eff} yielding numerical results that would fit the experimental data. When using air as the dissipative media, the calibration process also accounted for convection effects using an “equivalent conductivity.” To this end one can take advantage of the definition of the Nusselt number (Nu) and introduce an augmented thermal conductivity k^+ that will have the same effect as if one considers heat transfer convection instead, i.e., $k^+ = Nu \cdot k_{\text{air}} = hL$, where h is the convective heat transfer coefficient and L is a characteristic length. The numerical results for the temperatures that best matched the experimental measurements are included in Figs. 5 and 6 (dashed lines); these were obtained using $\eta_{\text{eff}} = 0.245$ and $Nu=1.2$ in air. Agreement between the numerical and the experimental values is very good for the case of water; in contrast, the agreement with the temperatures in air is only qualitative because heat dissipation in the radial direction is always stronger in the experiments. An important source for these discrepancies is related to the convective effects in the surrounding media, which can be generally difficult to simulate. Nonetheless, a quantitative agreement is more relevant for the case of water since biological tissues most often have high water contents.

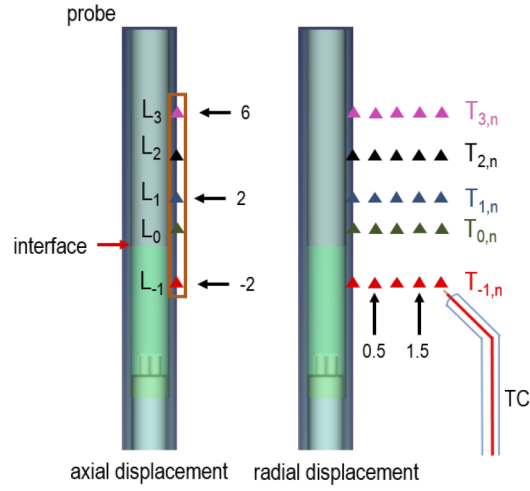


Fig. 4. Layout of the 5×5 matrix points within the vicinity of the FOPP. The temperature was measured at each point with a thermocouple (TC) and the interface between the PDMS-NaYF (green) and PDMS-CNP (gray) regions selected as the reference point ($z = 0$). The numbers indicate distances from the reference point in millimeters; $T(m, n)$ denotes the temperature at the m th-row and n th-column.

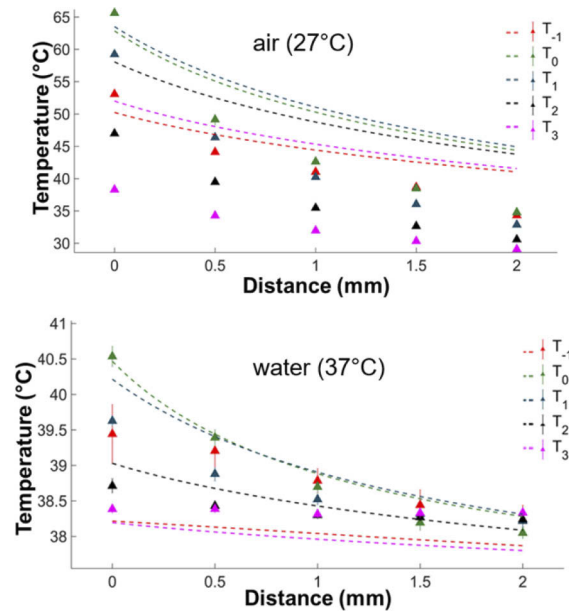


Fig. 5. Temperature values measured in air and water as a function of the radial distance for different axial positions (see Fig. 4 for reference positions). Symbols are experimental data while dashed lines are numerical values. $P_0 = 260\text{mW}$.

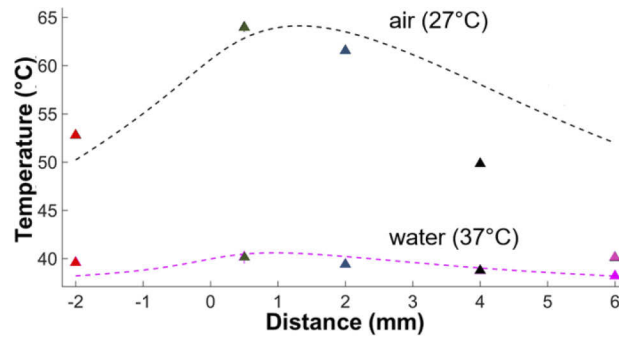


Fig. 6. Temperature values measured in air and water as a function of the axial distance (see Fig. 4 for reference positions). Symbols are experimental data with the same meaning as Fig. 4 and 5, while dashed lines are numerical values ($P_0 = 260\text{mW}$).

Figure 7 shows the numerical temperature contours in the vicinity of the FOPP obtained using $\eta_{\text{eff}} = 0.245$ as determined from the calibration procedure and for an optical power $P_0 = 260\text{ mW}$. Results are shown for three different dissipative media: water, air and skin. For skin we used $k = 0.37\text{ W/(m K)}$ and a far temperature field of 37 °C . In order to visualize the zones outside the probe that reach a hallmark temperature for hyperthermia treatments (e.g., $T = 41\text{ °C}$ for fever-range hyperthermia), we imposed a lower bound of $T = 41\text{ °C}$ in the plots shown in Figs. 7(a)–7(c) (see the color scale bars). Notice that in the case of skin and air, the FOPP indeed generates an isothermal envelope of 41 °C outside the glass casket, i.e., in the tissue domain; for skin in particular, the heated surface area is $\sim 30\text{ mm}^2$. In contrast, the $T = 41\text{ °C}$ isotherm extends further in air due to the lower dissipation or higher accumulation of heat. Due to the relatively high thermal conductivity of water ($k \sim 0.6\text{ W/(m K)}$), the 41 °C isotherm in this case is obtained within the external wall of the FOPP (i.e., the glass capillary). This indicates that our FOPP will generate, in general, very local zones with $T > 41\text{ °C}$ for optical powers $\sim 260\text{ mW}$ in tissues with thermal conductivities lower than water (human liver ~ 0.5 , human lung ~ 0.39 , adenocarcinoma of human breast ~ 0.41 , human myocardium ~ 0.49 , human fat ~ 0.2 and human muscle $\sim 0.38\text{ W/(m K)}$ are some examples [41–43]). The probe acts as a heat source that will increase the temperature of its surroundings through heat transfer. Thus, there is an interplay between the optical power and the thermal conductivity of the target tissue: for a given optical power, tissues with higher thermal conductivities will yield lower steady state temperatures because more heat will be dissipated.

A better insight of the temperature variations around the heating zone of the probe can be obtained upon analyzing the gradients. As an example, Fig. 7(d) shows the magnitude of the temperature gradient (∇T) near the FOPP for the case of skin as the dissipative medium. Clearly, the temperature decreases in regions away from the center of the probe (see the color scale bar). Physically, this implies that the rate of change in temperature as a function of the position is very large near the polymer composites' interface (indicated by the red arrow in Fig. 7(a)). For this particular case, the temperature gradient is on average $\sim 30\text{ °C/mm}$, with a maximum of $\sim 60\text{ °C/mm}$ in the center of the FOPP (i.e., a variation of 10 °C every 160 microns !). This brings back the idea that one should not assume that the temperature reported by the probe sensor is the same as the effective temperature maintained at the target point.

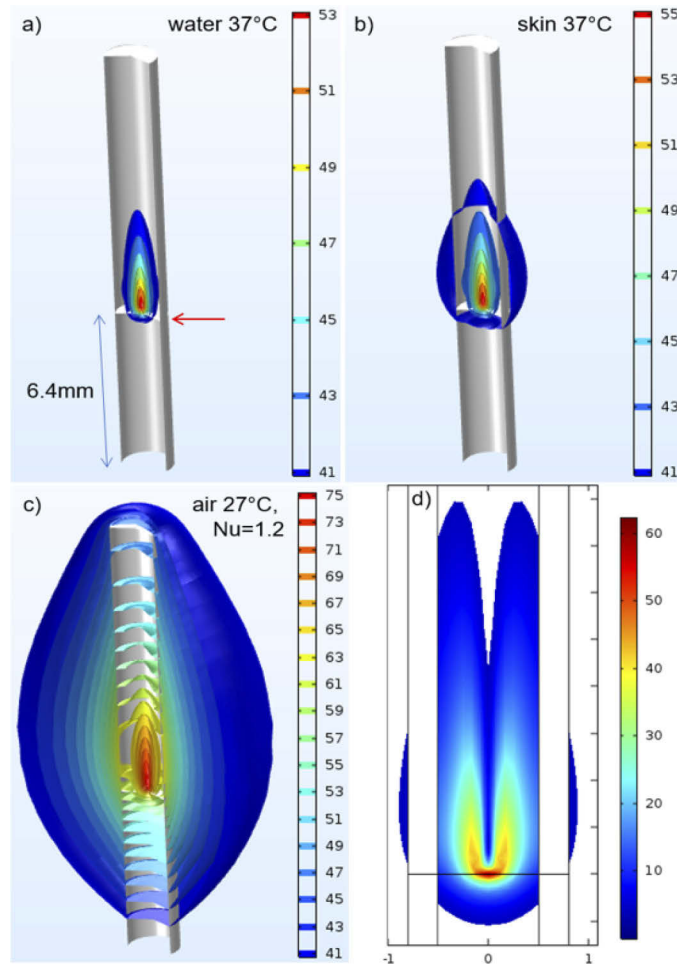


Fig. 7. 3D numerical isotherms of the FOPP surrounded by water (a), skin (b) and air (c) for $P_0 = 260$ mW. The dark blue outermost contours delimit the zone reaching a temperature of 41°C (values are in $^\circ\text{C}$); the polymer composites' interface located inside the probe is indicated with a red arrow in (a) (see [Visualization 1](#) for an animation of the time evolution of the isotherms). (d) 2D temperature gradient ($^\circ\text{C}/\text{mm}$) for the FOPP inside skin.

5. Proof of concept in agar phantom

To verify the potential of the FOPP for hyperthermia applications we used a standard agar phantom; this model has been used to mimic thermal properties of liver tissue as well as to test fiber optic devices intended for thermal therapies [36]. The phantom was prepared by dissolving agar powder in distilled water at 90°C (5% in weight) and the mix was poured in a disk mold and left to cool down for 25 min. The resulting agar disks (8 cm diameter and 4 mm height) were used within 90 min of fabrication to prevent water evaporation.

The thermal effects generated by the FOPP were evaluated upon placing it between two agar disks, as shown in Fig. 8, aiming at recreating a similar environment to those typically found in a therapeutic thermal procedure [36–38]. For comparative purposes and for assessing the temperature at different locations simultaneously, we placed a thermocouple (TC, K-type, Omega 5TC-TT-KI) and a fiber optic temperature sensor (FOTS, fiber Bragg grating) next to the probe. In addition, a second TC (TC agar) was located in the agar phantom displaced 5 mm away from

the polymer composites' interface (see Fig. 8). The increase in temperature registered in three experiments by the different sensors and for different output powers from the laser diode are shown in Fig. 9(a). During these experiments, the optical power was increased in three times intervals of 7 minutes each, until reaching a maximum of $P_0 = 260$ mW for a total experimental time of 21 minutes (the intermediate powers of 140 and 200 mW were selected arbitrarily). As seen in the plot, the temperature registered by the FOPP nicely tracks the readings from the TC placed close to the probe in this agar phantom model. In contrast, the temperatures registered by the fiber temperature sensor (FOTS) and the other TC placed in the agar sample (TC agar) clearly show smaller values than those acquired with the FOPP. This again confirms the strong temperature gradients obtained with the proposed device. Notice that the target temperature can be readily adjusted upon changing the optical power: initially, the probe shows a fast transient response and within 1 minute reaches a temperature plateau as typically observed in dynamic temperature measurements. Evidently, the steady state temperature will depend on the optical power and, as discussed below, on the thermal properties of the external medium (in this case, agar).

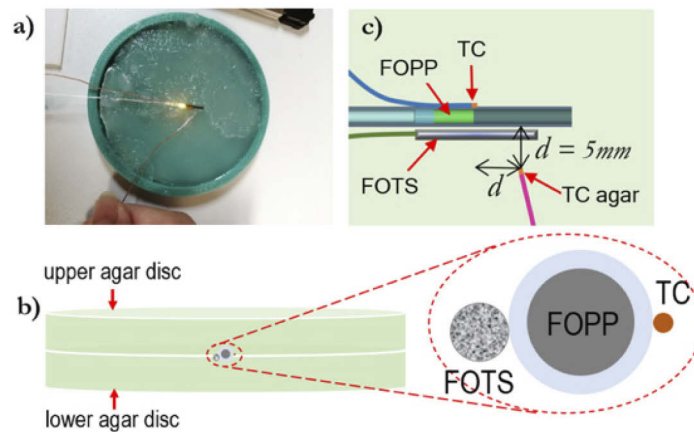


Fig. 8. Setup used for evaluating the FOPP performance in agar (agar disk dimensions: 8 cm diameter, 4 mm height). Top view image of the setup showing the probe and the temperature sensors placed on top of the agar disk (a); schematic (not to scale) showing the location of the thermocouples (TC), the photothermal probe (FOPP) and the fiber temperature sensor (FOTS) allocated between two agar disks (b); detailed side view (not to scale) of the location of the sensors and the FOPP (c).

In Fig. 9b we have further included the numerical results obtained for the transient temperature within the computational domain of the PDMS-NaYF composite. The solid line represents the temperature average obtained at the interface (surface average) between the domains of both polymer composites (i.e., PDMS-NaYF and PDMS-CNP), while the dashed line represents the temperature average obtained at the whole domain (volume average) of the PDMS-NaYF section. Clearly, the numerical surface average is closer to the experimental temperature obtained with the fluorescent polymer composite contained in the FOPP. The numerical volume average seems to underestimate the temperature by giving more weight to regions located far from the heat generation zone. However, it may also show further evidence of the highly localized heat generation that can be achieved with the proposed FOPP. In any case, the numerical surface average seems to provide a more appropriate way to represent the actual temperature reported by the sensor contained within the probe. It is also interesting to note that the temperature reading from the FOPP is indeed influenced by the thermal features of the surrounding medium (see Figs. 5 and 6). Given the strong temperature gradients obtained with this device, the temperature

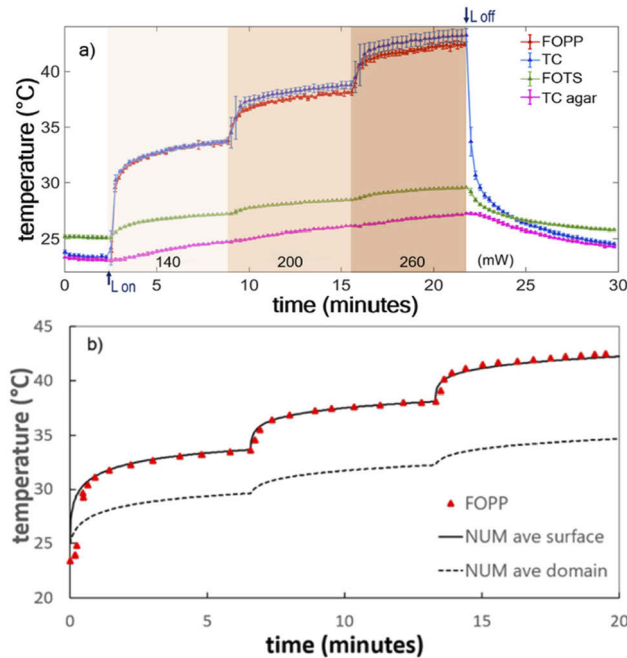


Fig. 9. (a) Temperature evolution in the agar disk following an increase of the optical power from 140 to 260 mW in three steps of 7 minutes each. Symbols represent the average of the experimental temperatures registered in three experiments by both thermocouples (TC and TC agar), the photothermal probe (FOPP) and a fiber temperature sensor (FOTS) located in the agar disk as shown in Fig. 8 (the bars represent the standard deviation). (b) Numerical simulations for the surface average (solid line) and volume average (dashed line) obtained for the PDMS-NaYF numerical region.

reading from the probe should therefore be very close to the temperature attained by the target tissue in contact with the FOPP. Hence, the numerical model provides a means to predict the temperature at any point outside the probe for any given dissipative media using the temperature reported by the FOPP as reference. In fact, we can explore the inverse problem: instead of finding the temperature reached at the target tissue for certain operational conditions (e.g., optical power and k of the tissue), we can obtain the minimal optical power needed to reach a minimum of 41 °C (hyperthermia treatment) at the target tissue for a given k . Following this approach, we obtained the plot included in Fig. 10, in which the blue region denotes the effective optical power required to achieve the target temperature. For example, to reach a minimum of 41 °C in human lung tissue, an optical power $P_0 \sim 200$ mW is needed; to reach a minimum of 41 °C in brain tissue, $P_0 \sim 260$ mW; meanwhile, heating human fat will require a pump power $P_0 \sim 117$ mW. Hence, for a given optical power, a tissue with large thermal conductivity will reach hyperthermia temperatures, but for the same optical power, a tissue with a smaller k will reach higher temperatures. Notice also that a family of curves for different target temperatures can be easily obtained following the same approach. The numerical model can thus provide suitable guidelines for setting the operating conditions of the probe to reach a desired temperature in a specific tissue.

The proposed FOPP shows interesting features that seem to be adequate for hyperthermia procedures. As shown in our experimental results and through numerical analysis, it offers a novel means to deliver heat in highly localized areas. An important aspect related to the design of the probe is related to its scalability, as the temperatures achieved in the PDMS-CNP photothermal

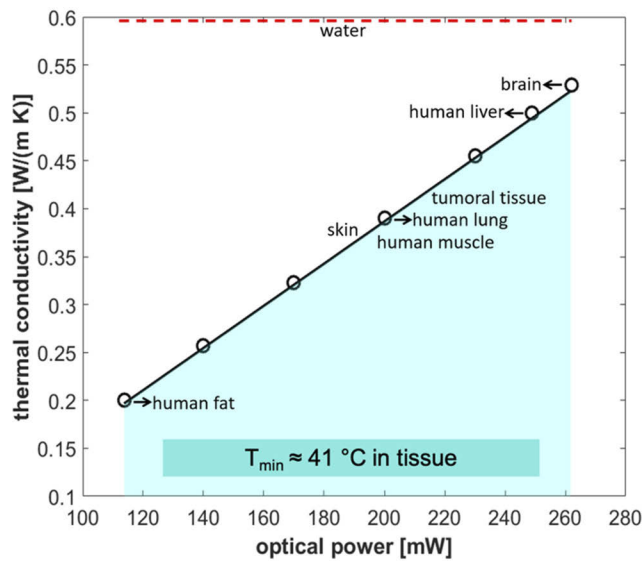


Fig. 10. Effective optical power (blue area) needed to reach a minimum of 41°C (hyperthermia treatment) for tissue with different thermal conductivities. For reference, the thermal conductivity of water is denoted by a dashed line.

composite can be increased upon changing the CNP concentration [40]. As seen from the numerical calculations, the photothermal effect is generated within the first few millimeters of the PDMS-CNP composite (see Fig. 7) thereby suggesting that the length of the FOPP could be reduced. Thus, optimization of the probe is still in place in order to obtain a suitable device for hyperthermia procedures in biomedical applications.

6. Conclusions

We have demonstrated a novel fiber optic photothermal probe (FOPP) capable to achieve temperatures within the ranges of interest for hyperthermia therapy. Heat is efficiently generated through photothermal effects in a polymer composite incorporating carbon nanoparticles, allowing for reaching temperatures $> 40^\circ\text{C}$ with optical powers within 260 mW, which are low compared to other approaches for realizing similar devices. Although the photothermal composite relies on carbon nanoparticles for efficient heat generation, these are contained within the probe in a polymer matrix, thereby avoiding their dissemination in the tissue and hence preventing any toxic effects associated with these exogenous absorbers. In contrast to other fiber-based probes, the thermal effects on the tissue are driven by heat transfer mechanisms rather than by optical absorption, thereby offering a novel means for performing thermal procedures in tissues with low optical absorption. Our results using an agar phantom showed that the FOPP provides good temperature stability in this medium, which is typically considered as a suitable biomimetic material for tissues with high water content.

Funding. Dirección General de Asuntos del Personal Académico, Universidad Nacional Autónoma de México (PAPIIT IG100519, PAPIIT IT100421); Consejo Nacional de Ciencia y Tecnología (Cátedras-CONACyT, FONCICYT 246648).

Acknowledgments. This work was partially funded by DGAPA-UNAM through PAPIIT, grants IG100519 and IT100421, and by CONACyT through grant FONCICYT 246648 and Cátedras-CONACyT program.

Disclosures. The authors declare no conflicts of interest.

Data availability. Data underlying the results presented in this paper are not publicly available at this time but may be obtained from the authors upon reasonable request.

References

1. E. van Sonnenberg, W. N. McMullen, and L. Solbiati, Eds. *Tumor Ablation: Principles and Practice* (Springer, 2005).
2. C. Christophi, A. Winkworth, V. Muralidharan, and P. Evans, "The treatment of malignancy by hyperthermia," *Surg. Oncol.* **7**(1-2), 83–90 (1998).
3. O. Nielsen, M. Horsman, and J. Overgaard, "A future for hyperthermia in cancer treatment?" *Eur. J. Cancer* **37**(13), 1587–1589 (2001).
4. G. F. Baronzio and E. D. Hager, "Introduction and Brief Historical Notes on Hyperthermia," in *Hyperthermia in Cancer Treatment: A Primer*, G. F. Baronzio and E. D. Hager, eds. (Landes Bioscience and Springer Science + Business Media, 2006).
5. K. Ahmed and S. Zaidi, "Treating cancer with heat: hyperthermia as promising strategy to enhance apoptosis," *J. Pak. Med. Assoc.* **63**(4), 504–508 (2013).
6. W. L. Titsworth, G. J. Murad, B. L. Hoh, and M. Rahman, "Fighting fire with fire: the revival of thermotherapy for gliomas," *Anticancer Res.* **34**(2), 565–574 (2014).
7. I. Mellal, A. Oukaira, E. Kengene, and A. Lakhssassi, "Thermal therapy modalities for cancer treatment: A review and future perspectives," *Appl. Sci. Res. Rev.* **4**(2), 14 (2017).
8. B. Hildebrandt, P. Wust, O. Ahlers, A. Dieing, G. Sreenivasa, T. Kerner, R. Felix, and H. Riess, "The cellular and molecular basis of hyperthermia," *Crit. Rev. Oncol. Hemat.* **43**(1), 33–56 (2002).
9. E. Schena, P. Saccomandi, and Y. Fong, "Laser ablation for cancer: past, present and future," *J. Funct. Biomater.* **8**(2), 19 (2017).
10. J. Beik, Z. Abed, F. S. Ghoreishi, S. Hosseini-Nami, S. Mehrzadi, A. Shakeri-Zadeh, and S. K. Kamrava, "Nanotechnology in hyperthermia cancer therapy: from fundamental principles to advanced applications," *J. Controlled Release* **235**, 205–221 (2016).
11. P. Cherukuri, E. Glazer, and S. Curley, "Targeted hyperthermia using metal nanoparticles," *Adv. Drug Delivery Rev.* **62**(3), 339–345 (2010).
12. X. Huang, P. K. Jain, I. H. El-Sayed, and M. El-Sayed, "Plasmonic photothermal therapy (PPTT) using gold nanoparticles," *Laser Med. Sci.* **23**(3), 217–228 (2008).
13. R. Singh and S. V. Torti, "Carbon nanotubes in hyperthermia therapy," *Adv. Drug Delivery Rev.* **65**(15), 2045–2060 (2013).
14. Z. Ashikbayeva, D. Tosi, D. Balmassov, E. Schena, P. Saccomandi, and V. Inglezakis, "Application of nanoparticles and nanomaterials in thermal ablation therapy of cancer," *Nanomaterials* **9**(9), 1195 (2019).
15. T. Fernández-Cabada, C. Sánchez-López de Pablo, A. Martínez-Serrano, F. D. Pozo-Guerrero, J. Serrano-Olmedo, and M. R. Gómez, "Induction of cell death in a glioblastoma line by hyperthermic therapy based on gold nanorods," *Int. J. Nanomed.* **7**, 1511–1523 (2012).
16. A. Burke, X. Ding, R. Singh, R. A. Kraft, N. Levi-Polyachenko, M. N. Rylander, C. Szot, C. Buchanan, J. Whitney, J. Fisher, and H. C. Hatcher, "Long-term survival following a single treatment of kidney tumors with multiwalled carbon nanotubes and near-infrared radiation," *Proc. Natl. Acad. Sci.* **106**(31), 12897–12902 (2009).
17. W. Zhang, Z. Guo, D. Huang, Z. Liu, X. Guo, and H. Zhong, "Synergistic effect of chemo-photothermal therapy using PEGylated Graphene oxide," *Biomaterials* **32**(33), 8555–8561 (2011).
18. X. Li, M. Takashima, E. Yuba, A. Harada, and K. Kono, "PEGylated PAMAM dendrimer-doxorubicin conjugate-hybridized gold nanorod for combined photothermal-chemotherapy," *Biomaterials* **35**(24), 6576–6584 (2014).
19. T. Menovsky, J. F. Beek, M. J. van Germet, F. X. and S. and G. Bown, "Interstitial laser thermotherapy in neurosurgery: a review," *Acta Neurochir.* **138**(9), 1019–1026 (1996).
20. S. Missios, K. Bekelis, and G. H. Barnett, "Renaissance of laser interstitial thermal ablation," *Neurosurgical Focus* **38**(3), E13 (2015).
21. D. Silva, M. Sharma, and G. H. Barnett, "Laser ablation vs open resection for deep-seated tumors: evidence for laser ablation," *Neurosurgery* **63**(CN_suppl_1), 15–26 (2016).
22. P. Wust, B. Hildebrandt, G. Sreenivasa, B. Rau, J. Gellermann, H. Riess, R. Felix, and P. M. Schlag, "Hyperthermia in combined treatment of cancer," *The Lancet Oncology* **3**(8), 487–497 (2002).
23. P. Saccomandi, E. Schena, and S. Silvestri, "Techniques for temperature monitoring during laser-induced thermotherapy: an overview," *Int. J. Hyperthermia* **29**(7), 609–619 (2013).
24. C. L. West, A. C. V. Doughty, K. Liu, and W. R. Chen, "Monitoring tissue temperature during photothermal therapy for cancer," *J. bio-X Res.* **2**(4), 159–168 (2019).
25. D. Polito, M. Arturo Caponero, A. Polimadei, P. Saccomandi, C. Massaroni, S. Silvestri, and E. Schena, "A needlelike probe for temperature monitoring during laser ablation based on fiber Bragg grating: Manufacturing and characterization," *J. Med. Devices* **9**(4), 041006 (2015).
26. E. Schena, D. Tosi, P. Saccomandi, E. Lewis, and T. Kim, "Fiber optic sensors for temperature monitoring during thermal treatments: an overview," *Sensors* **16**(7), 1144 (2016).
27. S. Korganbayev, A. Orrico, L. Bianchi, M. De Landro, A. Wolf, A. Dostovalov, and P. Saccomandi, "Closed-loop temperature control based on fiber bragg grating sensors for laser ablation of hepatic tissue," *Sensors* **20**(22), 6496 (2020).
28. L. Bianchi, S. Korganbayev, A. Orrico, M. De Landro, and P. Saccomandi, "Quasi-distributed fiber optic sensor-based control system for interstitial laser ablation of tissue: theoretical and experimental investigations," *Biomed. Opt. Express* **12**(5), 2841–2858 (2021).

29. P. J. Milne, J.-M. Parel, F. Manns, D. B. Denham, X. Gonzalez-Cirre, and D. S. Robinson, "Development of stereotactically guided laser interstitial thermotherapy of breast cancer: in situ measurement and analysis of the temperature field in ex vivo and in vivo adipose tissue," *Lasers Surg. Med.* **26**(1), 67–75 (2000).
30. S. A. van Nimwegen, H. F. L'Eplattenier, A. I. Rem, J. J. van der Lugt, and J. Kirpensteijn, "Nd:YAG surgical laser effects in canine prostate tissue: temperature and damage distribution," *Phys. Med. Biol.* **54**(1), 29–44 (2009).
31. Monteris Medical, "Neuroblate® System Disposables," Monteris Medical, 2020. [Online]. Available: <https://www.monteris.com/healthcare-professionals/neuroblate-system/neuroblate-system-disposables/>. [Accessed March 9, 2020].
32. C. Lagman, L. K. Chung, P. E. Pelargos, N. Ung, T. T. Bui, S. J. Lee, B. L. Voth, and I. Yang, "Laser neurosurgery: A systematic analysis of magnetic resonance-guided laser interstitial thermal therapies," *J. Clin. Neurosci.* **36**, 20–26 (2017).
33. P. Saccomandi, E. Schena, M.A. Caponero, R. Gassino, J. Hernandez, G. Perrone, A. Vallan, M. Diana, G. Costamagna, and J. Marescaux, "Novel carbon fiber probe for temperature monitoring during thermal therapies," in *2017 39th Annual International Conference of the IEEE Engineering in Medicine and Biology Society (EMBC)*, Seogwipo, South Korea, 873–876 (2017).
34. I. F. Saxena, K. Hui, and M. Astrahan, "Polymer coated fiber Bragg grating thermometry for microwave hyperthermia," *Med. Phys.* **37**(9), 4615–4619 (2010).
35. D. Tosi, E. G. Macchi, M. Gallati, G. Braschi, A. Cigada, S. Rossi, G. Leen, and E. Lewis, "Fiber-optic chirped FBG for distributed thermal monitoring of ex-vivo radiofrequency ablation of liver," *Biomed. Opt. Express* **5**(6), 1799–1811 (2014).
36. R. Gassino, Y. Liu, M. Konstantaki, A. Vallan, S. Pissadakis, and G. Perrone, "A fiber optic probe for tumor laser ablation with integrated temperature measurement capability," *J. Lightwave Technol.* **35**(16), 3447–3454 (2017).
37. T. Matta, H. Fukano, and S. Taue, "Simultaneous operation of laser ablation and temperature monitor using single optical fiber for hyperthermia," in *2017 Conference on Lasers and Electro-Optics Pacific Rim*, Singapore, Singapore, paper s1661 (2017).
38. S. A. Alqarni, W. G. Willmore, J. Albert, and C. W. Smelser, "Self-monitored and optically powered fiber-optic device for localized hyperthermia and controlled cell death in vitro," *Appl. Opt.* **60**(8), 2400–2411 (2021).
39. S. Sánchez-Escobar and J. Hernández-Cordero, "Fiber optic fluorescence temperature sensors using up-conversion from rare-earth polymer composites," *Opt. Lett.* **44**(5), 1194–1197 (2019).
40. R. Pimentel-Domínguez, A. M. Velázquez-Benítez, J. R. Vélez-Cordero, M. Hautefeuille, F. Sánchez-Arévalo, and J. Hernández-Cordero, "Photothermal effects and applications of polydimethylsiloxane membranes with carbon nanoparticles," *Polymers* **8**(4), 84 (2016).
41. H. S. Hatfield and L. G. C. Pugh, "Thermal conductivity of human fat and muscle," *Nature* **168**(4282), 918–919 (1951).
42. R. C. Webb, A. P. Bonifas, A. Behnaz, Y. Zhang, K. J. Yu, H. Cheng, M. Shi, Z. Bian, Z. Liu, Y. S. Kim, and W. H. Yeo, "Ultrathin conformal devices for precise and continuous thermal characterization of human skin," *Nat. Mater.* **12**(10), 938–944 (2013).
43. C. Rossmann and D. Haemmerich, "Review of temperature dependence of thermal properties, dielectric properties, and perfusion of biological tissues at hyperthermic and ablation temperatures," *Crit. Rev. Biomed. Eng.* **42**(6), 467–492 (2014).